

Intermediate Domain-guided Adaptation for Unsupervised Chorioallantoic Membrane Vessel Segmentation

Pengwu Song, Liang Xu, Peng Yao, Shuwei Shen, Pengfei Shao, Mingzhai Sun, and Ronald X. Xu

Abstract—The chorioallantoic membrane (CAM) model is widely employed in angiogenesis research, and distribution of growing blood vessels is the key evaluation indicator. As a result, vessel segmentation is crucial for quantitative assessment based on topology and morphology. However, manual segmentation is extremely time-consuming, labor-intensive, and prone to inconsistency due to its subjective nature. Moreover, research on CAM vessel segmentation algorithms remains limited, and the lack of public datasets contributes to poor prediction performance. To address these challenges, we propose an innovative Intermediate Domain-guided Adaptation (IDA) method, which utilizes the similarity between CAM images and retinal images, along with existing public retinal datasets, to perform unsupervised training on CAM images. Specifically, we introduce a Multi-Resolution Asymmetric Translation (MRAT) strategy to generate intermediate images to promote image-level interaction. Then, an Intermediate Domain-guided Contrastive Learning (IDCL) module is developed to disentangle cross-domain feature representations. This method overcomes the limitations of existing unsupervised domain adaptation (UDA) approaches, which primarily concentrate on directly source-target alignment while neglecting intermediate domain information. Notably, we create the first CAM dataset to validate the proposed algorithm. Extensive experiments on this dataset show that our method outperforms compared approaches. Moreover, it achieves superior performance in UDA tasks across retinal datasets, highlighting its strong generalization capability. The CAM dataset and source codes are available at <https://github.com/Light-47/IDA>.

Index Terms—Contrastive learning, self-training, synthetic data, unsupervised domain adaptation, vessel segmentation.

This work was supported by the National Key RD Program of China (Grant No. 2022YFA1104800) and the Anhui Provincial Natural Science Foundation (Grant No. 2308085MF219).

P. Song, L. Xu, M. Sun, S. Shen, and R. Xu are with the School of Biomedical Engineering, Division of Life Sciences and Medicine, University of Science and Technology of China, Hefei, Anhui, 230026, P.R. China and with the Suzhou Institute for Advanced Research, University of Science and Technology of China, Suzhou, Jiangsu, 215123, P.R. China (e-mail: {pwsong, xul666}@mail.ustc.edu.cn; {mingzhai, swshen, xux}@ustc.edu.cn).

P. Yao is with the School of Microelectronics, University of Science and Technology of China, Hefei 230026, China (e-mail: yaopeng@ustc.edu.cn).

P. Shao and R. Xu are with the Department of Precision Machinery and Precision Instrument, University of Science and Technology of China, Hefei 230026, China (e-mail: spf@ustc.edu.cn).

Pengwu Song and Liang Xu contributed equally to this work. Corresponding authors: Peng Yao, Shuwei Shen, and Ronald X. Xu.

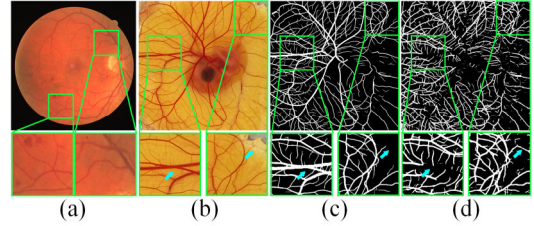


Fig. 1. A comparison between retinal and CAM vessels, along with an example of performance degradation when applying a model trained on retinal images to CAM images. (a) Source retinal images. (b) Target CAM images. (c) Annotations. (d) Predictions. Bottom left: under-segmentation. Bottom right: over-segmentation. The images below (a-d) show the corresponding enlarged views.

I. INTRODUCTION

ANGIOGENESIS is a strictly regulated process critical for embryonic development and plays a pivotal role in various pathophysiological conditions, such as wound healing, ischemic heart disease, and cancer [1]. One of the most widely used assays for studying angiogenesis is the developing chick embryo and its chorioallantoic membrane (CAM) [2]. Its popularity stems from several advantages, including the readily accessible experimental materials, short experimental duration, and the inherent immunodeficiency during the early stages of culture [3], [4]. Image segmentation enables the quantitative measurement of vascular surface area, length, and branching number, which are essential for assessing changes in angiogenic activity. Therefore, the accuracy of vessel segmentation in CAM images serves as the foundation for evaluating angiogenesis, providing critical insights into vascular development and pathology [5]. For example, tumors often promote vessel formation to support nutrient and waste transport, as well as gas exchange [6]. In hypoxic tumor microenvironments, tumors stimulate excessive angiogenesis via pro-angiogenic factors [7]. The CAM model, with its rich vascular network, is ideal for vascularization and angiogenesis studies. Combined with vessel segmentation, it quantifies tumor-induced vascular changes, offering key insights for anti-angiogenic drug evaluation.

In recent years, numerous studies [8]-[10] have designed vessel segmentation algorithms based on supervised deep learning, achieving promising results. However, these methods often require extensive pixel-level annotations and mainly focus on retinal vessel segmentation, with little attention to CAM vessels. Due to the dense vascular networks and strong branch connectivity in CAM images, vessel annotation is

highly time-consuming and labor-intensive. To our knowledge, no publicly available annotated CAM dataset has been released to date. If we apply the model trained on labeled source data (e.g., retinal images) directly to unlabeled target data like CAM images, it will lead to substantial performance degradation, as shown in Fig. 1, due to the notable discrepancies between the two image types.

Despite the significant image differences, can we leverage existing rich retinal datasets [11]-[13] to assist in training a high-performance CAM vessel segmentation model? To our knowledge, this is the first attempt to explore this approach. Typically, unsupervised domain adaptation (UDA) methods [14]-[20] are used for model transfer between domains with distribution gaps. UDA reduces the distribution gap between source and target domains, improving model generalization from labeled source data to unlabeled target data. However, if the gap is too large, UDA may fail, leading to poor target domain performance. To demonstrate the feasibility of this approach, we analyze both CAM and retinal images, highlighting their topological similarities, particularly in the publicly available DRIVE retinal dataset [11]. Based on these observations, we believe that employing UDA to aid in training a high-performance CAM segmentation model is a viable solution. To further validate this, we propose a novel Intermediate Domain-guided Adaptation (IDA) method for unsupervised vessel segmentation, constructing intermediate samples between retinal vessels and CAM vessels to reduce the domain shift problem. Extensive experiments confirm the effectiveness of our approach.

Early research on UDA segmentation tasks primarily focuses on reducing domain shifts through adversarial learning algorithms [14]-[16], [20]-[22]. Recently, to minimize visual appearance differences across domains, researchers utilize image translation techniques, such as the Copy-Paste (CP), which synthesizes intermediate images by integrating the visual style of one domain with the semantic information of the other [23], [24]. These simple CP methods not only effectively expand the dataset but also achieve the consistency regularization during model training. Moreover, when applied to UDA tasks, cross-domain CP can reduce domain shifts, further enhancing image-level adaptation. However, these methods are typically limited to intra-domain image generation or unidirectional translation between the source and target domains. This limitation results in insufficient utilization of intermediate domain information and suboptimal segmentation performance on the target domain [25], [26].

In addition, due to differences in image sizes between the source and target domains, as well as limitations in training resources and time, existing vessel segmentation methods [8]-[10] typically adopt one of the following two preprocessing strategies. The first approach downsamples images to a uniform size, which struggles to capture fine structures, resulting in the inability of basic CP techniques to address the issue of blurry predictions for thin vessels. The second approach crops the images into smaller patches, focusing only on local regions. This carries the risk of losing global information and may disrupt the continuity of thicker vessels. To overcome these

challenges, we propose a novel Multi-Resolution Asymmetric Translation (MRAT) strategy. By combining the aforementioned preprocessing methods with two different CP operations (CutMix [27] and ClassMix [28]), our approach effectively mitigates detail blurring, enhances vessel prediction continuity, while also achieving image-level adaptation.

To enhance feature expressiveness in the embedding space, contrastive learning has been widely applied into UDA [15], [16], [29]. These methods typically employ prototypes to establish unique latent representations for each class, thereby pulling features of the same class closer while pushing apart features of different classes. However, these methods mainly focus on single-domain representations, neglecting cross-domain feature distribution shifts. To address this problem, inspired by [18], we introduce an innovative Intermediate Domain-guided Contrastive Learning (IDCL) module, which leverages intermediate features to achieve both domain-level and feature-level adaptation.

To address the data scarcity, we create a CAM vessel dataset, named CAM_DB, comprising 40 images, of which 12 are annotated. To our knowledge, this is the first publicly available CAM vessel dataset. The release of this dataset is expected to advance the development of CAM vessel segmentation methods. We conduct extensive experiments on the DRIVE \rightarrow CAM_DB task and compare the performance of our approach with several well-known UDA methods. Furthermore, to validate the generalization capability of our method, we also perform UDA experiments across different retinal datasets. The results show that our IDA achieves the best performance.

The main contributions are summarized as follows:

- 1) We propose a novel IDA method aimed at addressing challenges such as limited images and lack of labels in the CAM vessel segmentation task. To our knowledge, this is the first work to leverage labeled retinal images and unlabeled CAM images to assist in training a high-performance CAM vessel segmentation model.
- 2) Additionally, we are the first to generate intermediate images at different resolutions in the unsupervised vessel segmentation domain. This enables image-level cross-domain interaction, allowing the model to balance both the overall and detailed vascular structures effectively.
- 3) To enhance feature discriminability, we design an IDCL module. This approach mitigates inter-domain discrepancies, facilitating effective feature-level adaptation without the need to explicitly minimize domain distances in the feature space.
- 4) To advance research on CAM vessel segmentation algorithms, we create the first publicly available CAM dataset. Our method achieves state-of-the-art performance on the DRIVE \rightarrow CAM_DB task. Furthermore, it shows superior performance over existing methods when applied to UDA tasks across retinal datasets.

II. RELATED WORK

A. Vessel Segmentation

- 1) *Traditional Methods*: Traditional vessel segmentation algorithms, such as matched filtering [30], adaptive threshold

[31], and adaptive tracking [32], typically use morphological features or pixel intensity as reference indicators. As for CAM vessel, Doukas *et al.* introduced an adaptive thresholding quantification algorithm [2]; Bibiloni *et al.* proposed a fuzzy mathematical morphology-based segmentation method [33]. Despite making significant progress, these methods often rely on predefined prior knowledge and require different parameter settings for each dataset.

2) *Deep Learning Methods*: Unlike conventional methods, deep learning approaches can automatically generate segmentation reference indicators by combining features from different dimensions. For example, Yan *et al.* [34] combined segment-level and pixel-level loss functions to learn more effective features for vessel segmentation, achieving a better balance between thick and thin vessels. Furthermore, Galdran *et al.* [9] proposed a simple cascaded network architecture based on U-Net [35], demonstrating its superiority through extensive experiments. Building on the network proposed in [9], Tan *et al.* [10] developed a skeleton fitting module to preserve vessel morphology, and employed a contrastive loss to enhance the distinction between vessels and the background. However, these methods typically require a large amount of labeled data. Due to the domain shift, the trained models often struggle to generalize to other vessel datasets. As a result, researchers have increasingly turned to UDA-based methods for unlabeled vessel segmentation, which have demonstrated promising results [20], [24], [36].

B. Unsupervised Domain Adaptation

Unsupervised Domain Adaptation (UDA) aims to utilize source domains with abundant labeled data to address tasks on unlabeled target domains. Existing UDA methods address the domain shift problem from two perspectives: image-level domain adaptation [18], [23], [37] and feature-level domain adaptation [15]-[17], [38], [39]. Image-level domain adaptation attempts to align inter-domain distributions based on certain visual representations, such as the image style. For example, Yang *et al.* [23] proposed using Fourier transforms to construct an intermediate domain to reduce the domain gap. In contrast, Na *et al.* [37] introduced a fixed-ratio MixUp [40] to enhance multiple intermediate domains, addressing the large domain gap in UDA scenarios. Feature-level domain adaptation tries to align feature distributions in the embedding space. Chen *et al.* [39] used adversarial learning on synthetic images to enhance feature invariance. Cheng *et al.* [38] proposed adaptive ClassMix [28] for bidirectional translation, using two complementary paths for domain adaptation. Meanwhile, Feng *et al.* [15] introduced a semantic alignment module to minimize same-class prototype distances for feature-level adaptation. Although numerous studies have applied UDA to vessel segmentation tasks [20], [24], [41], existing methods fail to adequately address the significant distribution differences caused by cross-species vessel data, resulting in insufficient cross-domain semantic consistency. Additionally, these methods have limited ability to represent fine structures, such as capillaries. To address this challenge, we propose a novel Intermediate Domain-guided Adaptation (IDA) method that

leverages labeled retinal images and unlabeled CAM images for training, aiming to enhance inter-domain information interaction and improve the representation of fine image structures.

C. Contrastive Learning

Contrastive learning aims to bring same-class features closer and push different-class features apart in the embedding space, improving intra-class compactness and inter-class separation. It has been widely used in UDA [16], [18], [19], [29], proving its effectiveness. Liu *et al.* [16] proposed a margin-preserving contrastive loss by introducing a deviation angle as a penalty for positive anchors to enhance inter-class differences. Kuang *et al.* [19] extended the contrastive loss by combining pixel-to-pixel, pixel-to-prototype, and prototype-to-prototype contrasts to better utilize the underlying semantic information at different levels. However, existing methods focus on obtaining better discriminative representations within a single domain while neglecting inter-domain feature differences. Although Lu *et al.* [18] proposed a domain-interactive contrastive learning module that incorporates cross-domain alignment into the feature space, directly using source and target domain prototypes cannot fully eliminate the domain shift. To address this, we propose an intermediate domain-guided contrastive learning module, which leverages intermediate features to guide cross-domain feature alignment.

III. METHODOLOGY

A. Framework Overview

The flowchart of our IDA method is illustrated in Fig. 2, which employs the teacher-student architecture [42] as the basic framework. The student and teacher models share the same initialization, which is derived from pre-training on the source dataset. During training, the teacher model is updated by the student model using the Exponential Moving Average (EMA) strategy [42]. We use φ_t, φ_s to represent the parameters of the teacher model and the student model, respectively. The parameters of the teacher model are updated as follow:

$$\varphi_t^{(k)} \leftarrow \lambda \varphi_t^{(k-1)} + (1-\lambda) \varphi_s^{(k)}, \quad (1)$$

where k denotes the number of iterations. λ is a momentum parameter. In this work, λ is fixed to 0.99.

Considering accuracy and flexibility, we utilize cascaded U-Nets (W-Net) [9] as our backbone. The training set consists of a labeled source dataset $D^s = \{x_s^i, y_s^i\}_{i=1}^N$ with N retinal images and an unlabeled target dataset $D^t = \{x_t^i\}_{i=1}^M$ with M CAM images, where x_s^i and x_t^i denote the i -th sample from the source and target domains, respectively, and y_s^i represents the corresponding ground truth from the source domain. The training process can be summarized as follows: randomly select two source images $\{x_s^i, x_s^j\}$ and two target images $\{x_t^k, x_t^l\}$ from the training set. The four images are then processed through the multi-resolution asymmetric translation strategy to generate two intermediate images $\{x_{t2s}, x_{s2t}\}$, which are input

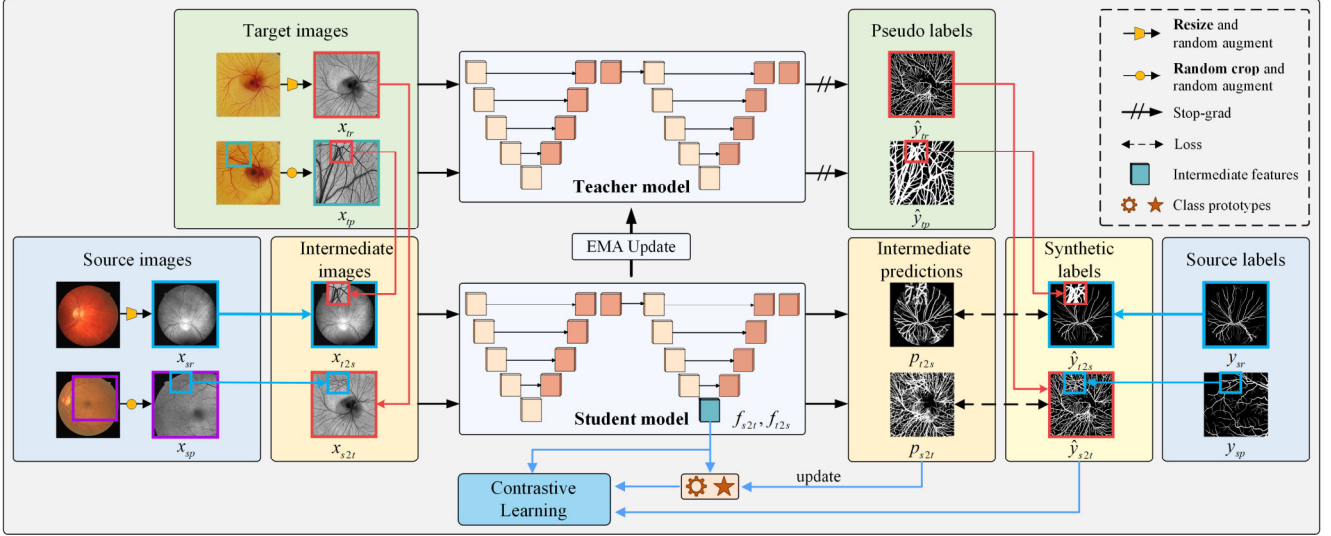


Fig. 2. Framework of proposed method comprising two innovative components: (1) A multi-resolution asymmetric translation strategy that employs images of different resolutions for cross-domain transformation to generate intermediate images, facilitating image-level domain adaptation. (2) An intermediate domain-guided contrastive learning module, which adaptively updates prototypes using intermediate features and performs cross-domain contrastive learning with the intermediate prototypes to reduce domain gaps at the feature level.

to the student model. Simultaneously, the transformed target images are fed into the teacher model to generate pseudo-labels. These pseudo-labels are combined with source labels to produce synthetic labels $\{\hat{y}_{r2s}, \hat{y}_{s2t}\}$, which guide the training of the student model. During training, we introduce an intermediate domain-guided contrastive learning module. This module utilizes the feature maps $\{f_{t2s}, f_{s2t}\}$ from the student model’s encoder and the predicted outputs $\{p_{r2s}, p_{s2t}\}$ from the student model’s decoder. to jointly update prototypes. Subsequently, the contrastive loss is calculated using the intermediate features to ensure that the network fully exploits intermediate domain information, achieving feature-level cross-domain alignment and reducing domain gaps.

B. Multi-Resolution Asymmetric Translation

Specifically, as shown in Fig. 2, for two randomly selected labeled source images $\{x_s^i, x_s^j\}$ and two unlabeled target images $\{x_t^k, x_t^l\}$ in the training set, we resize x_s^i and x_t^k to a uniform size of $W \times H \times D$, while randomly cropping x_s^j and x_t^l to the same size of $W \times H \times D$, where W , H , and D , represent height, width, and channel, respectively. Due to significant color differences between the source and target images (Fig. 1), which can affect model performance, we convert all images to grayscale to eliminate color bias, resulting in images of size $W \times H$. To further increase data diversity, we apply data augmentation techniques to these four images, such as random flipping and color jitter. After these transformations, the four images are represented as x_{sr}, x_{sp}, x_{tr} , and x_{tp} .

To align the distributions of the source and target domains, we generate intermediate images by randomly replacing a region of the target image with corresponding source image (or

vice versa), while keeping the resolution and overall size of the replaced images unchanged. In detail, we first create a CutMix mask M_R by randomly setting a region of size $m \times m$ ($m < \min\{W, H\}$) within an all-zero area of size $W \times H$ to 1. Then, we multiply the mask M_R with the ground truth y_{sp} of the source patch x_{sp} resulting in a foreground-class ClassMix mask M_C . The two intermediate images can then be generated using the following equations:

$$x_{t2s} = x_{tp} \odot M_R + x_{sr} \odot (\mathbf{1} - M_R), \quad (2)$$

$$x_{s2t} = x_{sp} \odot M_C + x_{tr} \odot (\mathbf{1} - M_C), \quad (3)$$

where $\mathbf{1} \in \{1\}^{W \times H}$, \odot means element-wise multiplication. These two intermediate images are then fed into the student model for training. Supervisory signals are also generated in a similar manner, as shown in the following equation:

$$\hat{y}_{t2s} = \hat{y}_{tp} \odot M_R + y_{sr} \odot (\mathbf{1} - M_R), \quad (4)$$

$$\hat{y}_{s2t} = y_{sp} \odot M_C + \hat{y}_{tr} \odot (\mathbf{1} - M_C), \quad (5)$$

where $\hat{y}_{t2s}, \hat{y}_{s2t}$ denote the synthetic labels of the intermediate images, y_{sr}, y_{sp} are the ground truths of x_{sr} and x_{sp} , and $\hat{y}_{tr}, \hat{y}_{tp}$ correspond to the pseudo-labels of x_{tr} and x_{tp} , which are obtained from the teacher model through an argmax operation followed by one-hot encoding.

Since the patches pasted in x_{t2s} and x_{s2t} are taken directly from x_{tp} and x_{sp} without downsampling the original images, thin vessel details are preserved. Meanwhile, the remaining regions are derived from x_{sr} and x_{tr} , retaining the overall structural information of the source and target images. Through these unique CP operations, our approach can efficiently

alleviate detail blurring and improve the continuity of vessel prediction. Additionally, it is worth noting that for x_{t2s} , since ground truths are unavailable, we employ a CutMix-like operation, directly pasting a patch from x_{tp} . For x_{s2t} , we use a ClassMix-like operation, pasting only the foreground from the patch of x_{sp} onto x_{tp} . This overlay of foregrounds from both x_{sp} and x_{tp} creates an interlacing effect of vessels, enabling the model to better handle such complex scenarios during training. The two intermediate images obtained by these two different methods serve two purposes: first, they enrich the diversity of the input and alleviate issues such as label blurring at the rectangular boundaries introduced by CutMix and the high accuracy requirement for labels in ClassMix. Second, they help reduce domain shifts from different perspectives. By applying consistency regularization with pseudo-labels during training, this approach enhances the model performance and generalization ability.

C. Intermediate Domain-guided Contrastive Learning

The MRAT strategy described above generates unique intermediate images to facilitate image-level adaptation, while our IDCL method leverages prototype-based contrastive learning to further achieve feature-level adaptation. Unlike previous work [16], [17], [19], which relies on source and target features, our method uses intermediate features to update prototypes and perform contrastive learning. As illustrated in Fig. 3, this approach not only achieves intra-class compactness and inter-class separability within each domain but also reduces domain gaps, promoting better inter-domain interaction. Specifically, we first obtain the initial prototypes $C^{(0)} = \{c_1^{(0)}, c_2^{(0)}, \dots, c_L^{(0)}\}$ by computing the class centers of the initial source pixel features from a pre-trained model on source images, where L denotes the total number of classes ($L = 2$ for the vessel segmentation task). The prototypes are defined as follows:

$$c_r^{(0)} = \frac{1}{|N_r|} \sum_{i=1}^N \sum_{j=1}^{h \times w} f_s^{i(0)}[j] \cdot \mathbb{I}(Y_s^i[j] = r), \quad (6)$$

where N represents the number of source samples. $f_s^{i(0)}$ denotes the feature map of the source image obtained through the pre-trained model, coming from the intermediate layer of the second U-net model in the backbone (as shown in the ‘‘Intermediate features’’ of Fig. 2). h, w are the height and width of the feature map, respectively. Y_s^i is obtained by downsampling the source label y_s^i to a size of $h \times w$. $\mathbb{I}(\circ)$ is the indicator function, which equals 1 if (\circ) is true. $|N_r|$ denotes the number of features belonging to the r -th class in the source domain, i.e. $|N_r| = \sum_{i=1}^N \sum_{j=1}^{h \times w} \mathbb{I}(Y_s^i[j] = r)$.

To enhance the representational ability of prototypes and align the source and target domains at the feature level, we use the features generated from the intermediate images to update the prototypes:

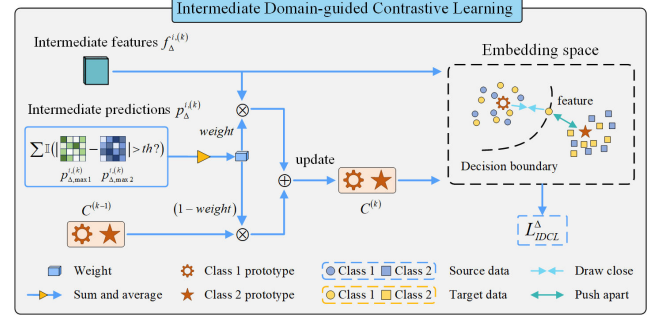


Fig. 3. The diagram of the intermediate domain-guided contrastive learning module. First, the update weights at the k -th iteration are computed using the predictions $p_A^{i(k)}$ of the intermediate images. The prototypes $c^{(k)}$ is then updated by the weights and intermediate features $f_A^{i(k)}$. Finally, calculate the contrastive loss.

$$c_r^{(k)} \leftarrow (1 - w_{t2s}^{(k)})c_r^{(k-1)} + w_{t2s}^{(k)}c_{r,t2s}^{(k)}, \quad (7)$$

$$c_r^{(k)} \leftarrow (1 - w_{s2t}^{(k)})c_r^{(k-1)} + w_{s2t}^{(k)}c_{r,s2t}^{(k)}, \quad (8)$$

where k denotes the k -th iteration during training. $c_r^{(k)}$ denotes the intermediate variable for the k -th update. $c_{r,t2s}^{(k)}, c_{r,s2t}^{(k)}$ represent the prototypes of the r -th class computed from intermediate source-like images and target-like images, while $w_{t2s}^{(k)}, w_{s2t}^{(k)}$ denote their respective update weights. These can be computed using the following formulas:

$$c_{r,\Delta}^{(k)} = \frac{1}{|B_{r,\Delta}|} \sum_{i=1}^{B_\Delta} \sum_{j=1}^{h \times w} f_\Delta^{i(k)}[j] \cdot \mathbb{I}(\hat{Y}_\Delta^{i(k)}[j] = r), \quad (9)$$

$$w_\Delta^{(k)} = \frac{1}{|B_\Delta|} \sum_{i=1}^{B_\Delta} \sum_{j=1}^{H \times W} \mathbb{I}(|p_\Delta^{i(k)}[j]_{\max 1} - p_\Delta^{i(k)}[j]_{\max 2}| > th), \quad (10)$$

where $\Delta \in \{t2s, s2t\}$. $f_\Delta^{i(k)}$ represents the feature map of the i -th intermediate image in each iteration. $\hat{Y}_\Delta^{i(k)}$ is obtained by downsampling the synthesized labels $\hat{y}_\Delta^{i(k)}$ to the size of $h \times w$. B_Δ represents the number of intermediate images in an iteration. In this paper, $B_{t2s} = B_{s2t}$, both of which are half the batch size. $|B_\Delta|$ indicates the total number of pixels in the predicted probability map for the entire batch of intermediate images, where $|B_\Delta| = B_\Delta \times H \times W$. $|B_{r,\Delta}|$ denotes the number of pixel features belonging to the r -th class in a batch of intermediate images, and $|B_{r,\Delta}| = \sum_{i=1}^{B_\Delta} \sum_{j=1}^{h \times w} \mathbb{I}(\hat{Y}_\Delta^{i(k)}[j] = r)$. $p_\Delta^{i(k)}$ represents the predicted probability map of the intermediate images, with the indices ‘‘max1’’ and ‘‘max2’’ referring to the maximum and submaximum predicted probability values, respectively. th is the threshold.

It can be observed that the update weight $w_\Delta^{(k)}$ is computed by considering only pixels with high prediction probability confidence. This approach aims to dynamically adjust $w_\Delta^{(k)}$ to mitigate the impact of unreliable pseudo-labels and features on the prototypes. When the model is initially transferred to the

intermediate domain for training, both the reliability of features and pseudo-labels are low due to the domain shift. In this case, $w_{\Delta}^{(k)}$ is relatively small, and the update of the prototypes is more conservative. As training progress, the reliability of features and pseudo-labels improves, leading to more high-confidence pixels. Consequently, as $w_{\Delta}^{(k)}$ increases, the prototypes can be updated more rapidly. By employing this dynamic prototype update method, we can obtain more expressive and generalized prototypes. Moreover, these intermediate prototypes are treated as the mean of the source and target domain features in the embedding space, which further guide subsequent contrastive learning to learn domain-invariant representations.

Given the prototype $c_r^{(k)}$ for class r and intermediate pixel features $f_{\Delta}^{i(k)}[j]$, their cosine similarity are defined as follows:

$$\cos(\theta_{\Delta}^{i(k)}[j, r]) = \frac{[c_r^{(k)}]^T f_{\Delta}^{i(k)}[j]}{\|c_r^{(k)}\|_2 \|f_{\Delta}^{i(k)}[j]\|_2}, \quad (11)$$

where $\|\cdot\|_2$ denotes the L_2 regularization. By calculating the cosine similarity, we can then obtain the contrastive loss for the i -th intermediate image, defined as:

$$L_{IDCL}^{\Delta} = -\sum_{j=1}^{h \times w} \log \frac{\exp(\cos(\theta_{\Delta}^{i(k)}[j, \hat{y}_j] + \delta)/\tau)}{\exp(\cos(\theta_{\Delta}^{i(k)}[j, \hat{y}_j] + \delta)/\tau) + S(j)}, \quad (12)$$

where $\cos(\theta_{\Delta}^{i(k)}[j, \hat{y}_j])$ indicates the cosine similarity between the pixel feature and positive anchor (i.e., positive pair). \hat{y}_j denotes the class of the j -th pixel. $S(j) = \sum_{r=1, r \neq \hat{y}_j}^L \exp(\cos(\theta_{\Delta}^{i(k)}[j, r])/\tau)$ is used for normalization.

Following MPSCL [16], δ represents the deviation angle penalty, which is used to preserve the margin of the positive prototype. The temperature τ is typically set to 1 by default.

The goal of L_{IDCL}^{Δ} is to minimize the distance between positive pairs and maximize the distance between negative pairs in the embedding space, as shown in the right part of Fig. 3. Furthermore, the strategy of guiding contrastive learning with intermediate prototypes leverages intermediate information, ensuring more consistent learning across the source and target domains, thereby promoting feature-level domain adaptation.

D. Training Objective

The loss for the intermediate samples during the training phase can be divided into three components: the supervised loss from the labeled source domain, the consistency loss from the unlabeled target domain, and the contrastive loss from the intermediate features. The supervised loss is further divided into the classification loss L_{cls}^s and segmentation loss L_{seg}^s , which can be expressed as:

$$L_{cls}^s = L_{cls}(p_{12s}, \hat{y}_{12s}) \odot (\mathbf{1} - M_R) + L_{cls}(p_{s2t}, \hat{y}_{s2t}) \odot M_C, \quad (13)$$

$$L_{seg}^s = L_{seg}(p_{12s}, \hat{y}_{12s}) \odot (\mathbf{1} - M_R) + L_{seg}(p_{s2t}, \hat{y}_{s2t}) \odot M_C, \quad (14)$$

where L_{cls} , L_{seg} represent the cross-entropy loss and DICE loss, respectively. The consistency loss L_{con} uses the Mean Squared Error (MSE) loss, defined as follows:

$$L_{con} = \text{MSE}(p_{s2t}, p_{tr}) \odot (\mathbf{1} - M_C) + \text{MSE}(p_{12s}, p_{tp}) \odot M_R, \quad (15)$$

where p_{tr} , p_{tp} represent the predicted probability maps of the target images x_{tr} and x_{tp} output by the teacher model.

In conclusion, the overall loss is summarized as follows:

$$L_{all} = \alpha_1 L_{cls}^s + \alpha_2 L_{seg}^s + \beta_1 L_{IDCL}^{12s} + \beta_2 L_{IDCL}^{s2t} + \gamma L_{con}, \quad (16)$$

where $\alpha_1, \alpha_2, \beta_1, \beta_2, \gamma$ are hyperparameters used to balance the training. In this work, both are set to 1.

IV. EXPERIMENTS

A. Experimental Setup

1) Datasets: In the experiments, we use three widely used retinal datasets—DRIVE [11], CHASEDB1 [12], STARE [13]—and a homemade CAM vessel dataset, CAM_DB. We conduct UDA tasks from DRIVE to CAM_DB. Additionally, to validate the generalization ability, we also perform experiments from DRIVE to CHASEDB1 and STARE. The detailed descriptions of each dataset are provided below.

DRIVE: The DRIVE dataset is a publicly available dataset consisting of 40 color retinal images, accompanied by 40 corresponding segmentation labels. Each image has a resolution of 584×565 . In our experiments, we uniformly use the DRIVE dataset as the source domain. We randomly select 36 images for the training set and the remaining 4 images for the validation set.

CHASEDB1: The CHASEDB1 dataset consists of 28 labeled images of both left and right eyes. Each image has a resolution of 999×960 . In this study, we use 21 images for the training set, with the remaining images used for testing.

STARE: The STARE dataset consists of 20 labeled retinal images, with a resolution of 700×605 . We use 15 images for the training set, with the remaining 5 images used for testing.

CAM_DB: After approximately 50 hours of incubation, we extract the embryos from the eggshells and place them in cups lined with plastic film. We then collect images of the chick embryos after 3 to 6 days of cultivation. The dataset consists of 40 color images, 12 of which are accompanied by pixel-level annotations. Each image has a resolution of 1024×1024 . We select 28 images for the training set, with the remaining 12 labeled unlabeled images used as the test set.

2) Evaluation Metrics: Following the previous work [8], [9], we adopt five metrics to evaluate algorithms performance: the area under the receiver operating characteristics curve (AUC), accuracy (ACC), sensitivity (SE), specificity (SP), and Dice score (DICE).

3) Implementation Details: The experimental setup in this paper is as follows: We use W-Net [9] for both student and teacher models. The batch size is set to 4. The optimizer is AdamW [43] with betas (0.9, 0.999) and a weight decay of $5e-4$. The learning rate is initially set to $2.5e-4$. In our MRAT

TABLE I
QUANTITATIVE RESULTS OF DIFFERENT METHODS ON THE DRIVE → CAM_DB TASK.

Methods	AUC	ACC	SE	SP	DICE
AdvEnt [14]	0.9533	0.9102	0.8314	0.9227	0.7165
MPSCL [16]	0.9702	0.9376	0.8348	0.9538	0.7849
SkelCon [10]	0.9784	0.9520	<u>0.8655</u>	0.9657	0.8312
SEASA [15]	0.9651	0.9330	0.8108	0.9524	0.7677
SePiCo [17]	0.9715	0.9500	0.8633	0.9637	0.8250
DCLPS [18]	<u>0.9843</u>	<u>0.9573</u>	0.8616	<u>0.9724</u>	<u>0.8463</u>
IDA(Ours)	0.9878	0.9641	0.9047	0.9735	0.8730

TABLE II
QUANTITATIVE RESULTS OF DIFFERENT METHODS ON THE DRIVE → CHASEDB1 TASK.

Methods	AUC	ACC	SE	SP	DICE
AdvEnt [14]	0.9396	0.9298	0.7574	0.9474	0.6667
MPSCL [16]	0.9622	0.9441	0.7974	<u>0.9591</u>	0.7254
SkelCon [10]	0.9667	0.9413	<u>0.8628</u>	0.9493	0.7315
SEASA [15]	0.9579	0.9414	0.7727	0.9586	0.7096
SePiCo [17]	0.9585	0.9418	0.8021	0.9561	0.7186
DCLPS [18]	<u>0.9755</u>	<u>0.9492</u>	0.8602	0.9583	<u>0.7584</u>
IDA(Ours)	0.9780	0.9520	0.8690	0.9605	0.7703

strategy, both the downsampled images and cropped patches from the source and target domains are of size 384×384 . During the testing phase, for the CAM dataset, we resize the original images to 512×512 . For the CHASEDB1 and STARE datasets, we resize the images to 384×384 before feeding them into the student model, and then use interpolation to restore the segmentation results to their original size.

B. Comparison with Existing Methods

To evaluate the performance of our model, we compare it with other state-of-the-art methods, including AdvEnt [14], MPSCL [16], SkelCon [10], SEASA [15], SePiCo [17], and DCLPS [18]. For a fair comparison, all methods are implemented using the original code and default settings, with the same backbone employed across all approaches.

1) *Results from DRIVE to CAM_DB*: Table I presents the quantitative results for CAM segmentation, where DRIVE serves as the source domain and CAM_DB as the target domain. The best result is highlighted in bold, while the second-best result is underlined. Our method demonstrates superior performance across five evaluation metrics, achieving a DICE score exceeding 0.87 and surpassing 0.90 in the remaining four metrics. This confirms the feasibility of transferring knowledge from retinal datasets to the CAM dataset. Moreover, our method consistently outperforms others, particularly in the DICE and SE metrics, where it demonstrates significant improvements of 2.67% and 3.92%, respectively, compared to the second-best results. These improvements demonstrate that our model effectively identifies vessel pixels in CAM images while filtering out non-vascular regions, thus mitigating both under-segmentation and overconfidence issues.

2) *Results from DRIVE to CHASEDB1 and STARE*: To further evaluate the effectiveness of our method and assess its

TABLE III
QUANTITATIVE RESULTS OF DIFFERENT METHODS ON THE DRIVE → STARE TASK.

Methods	AUC	ACC	SE	SP	DICE
AdvEnt [14]	0.9540	0.9250	0.8223	0.9362	0.6819
MPSCL [16]	0.9625	0.9426	0.8047	0.9576	0.7327
SkelCon [10]	0.9419	0.9428	0.8220	0.9558	0.7373
SEASA [15]	0.9537	0.9385	0.7921	0.9543	0.7156
SePiCo [17]	0.9490	0.9416	0.8014	0.9568	0.7284
DCLPS [18]	<u>0.9668</u>	<u>0.9526</u>	<u>0.8262</u>	<u>0.9663</u>	<u>0.7732</u>
IDA(Ours)	0.9758	0.9601	0.8328	0.9738	0.8030

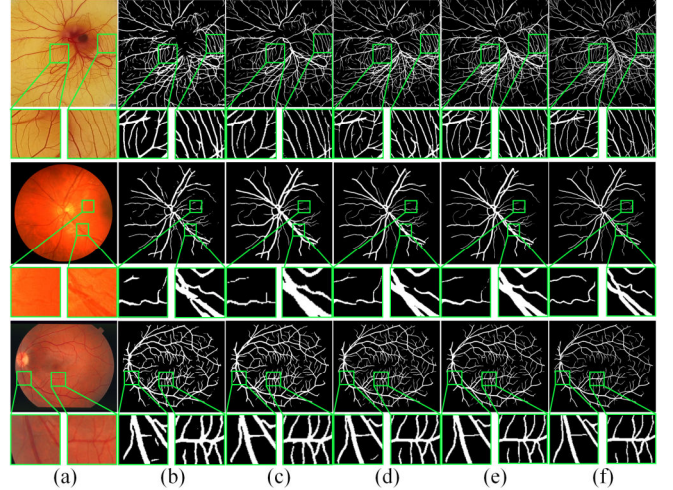


Fig. 4. Visualizes the segmentation results of different methods. (a) Original Images, (b) MPSCL [16], (c) SkelCon [10], (d) DCLPS [18], (e) Ours, (f) Annotations. From top to bottom: DRIVE → CAM_DB, DRIVE → CHASEDB1, and DRIVE → STARE. Below each image is an enlarged patch of the image.

generalization capability and robustness, we conduct experiments using CHASEDB1 and STARE as target domains. As shown in Table II and Table III, our method consistently outperforms other approaches on both datasets, particularly in the DICE metric, achieving improvements of 1.19% and 2.98%, respectively, over the second-best results. These findings highlight the effectiveness of our method in adapting to diverse UDA tasks while maintaining strong generalization and robustness. Notably, a comparison of Table I with Table II and Table III reveals that the results on CAM_DB are higher than those on CHASEDB1 and STARE. This further demonstrates the feasibility of transferring from retinal images to CAM images, with performance even surpassing that of transfer between different retinal datasets.

3) *Visualization*: Fig. 4 visualizes the segmentation results of different algorithms on the three transfer tasks: DRIVE → CAM_DB, DRIVE → CHASEDB1, and DRIVE → STARE. It can be observed that MPSCL [16] struggles with both over-segmentation and under-segmentation, leading to poor performance in segmenting large vessels. SkelCon [10] generally yields good results, but overconfident predictions result in vessel pixels being significantly larger than the actual labels. DCLPS [18] also suffers from the issue of disconnected vessel segmentation. In contrast, our method outperforms

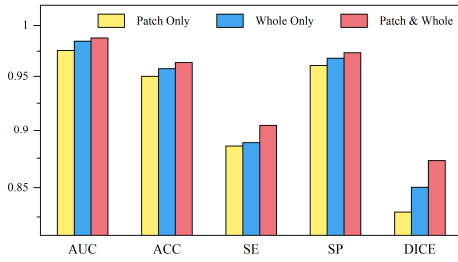


Fig. 5. Quantitative analysis of different input forms.

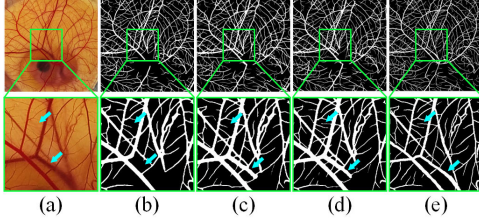


Fig. 6. Visualization comparison of different input strategies on the DRIVE → CAM_DB task. (a) Original Images, (b) Patch only, (c) Whole only, (d) Ours, (e) Annotations. Below each image is an enlarged patch of the image.

TABLE IV

ABLATIVE RESULTS OF EACH TRANSLATION SETTINGS IN OUR MODEL ON THE DRIVE → CAM_DB TASK. S2TCUT AND S2TCLASS REFER TO UNIDIRECTIONAL CUTMIX AND CLASSMIX FROM THE SOURCE DOMAIN TO THE TARGET DOMAIN, WHILE T2SCUT AND T2SCCLASS REPRESENT THE REVERSE DIRECTION, FROM THE TARGET DOMAIN TO THE SOURCE DOMAIN. BI-CUT AND BI-CLASS REPRESENT BIDIRECTIONAL CUTMIX AND CLASSMIX BETWEEN THE SOURCE AND TARGET DOMAINS, RESPECTIVELY.

Methods	Settings	AUC	ACC	SE	SP	DICE
UT	S2TCut	0.9805	0.9548	0.8534	0.9708	0.8374
	T2SCut	0.9778	0.9496	0.8301	0.9685	0.8181
	S2TClass	0.9816	0.9531	0.8727	0.9658	0.8354
	T2SClass	0.9792	0.9492	0.8424	0.9660	0.8189
BST	Bi-Cut	0.9815	0.9564	0.8513	0.9730	0.8421
	Bi-Class	0.9832	0.9561	0.8764	0.9686	0.8448
BAT	S2TCut & T2SClass	0.9878	0.9635	0.9052	0.9727	0.8713
	S2TClass & T2SCut	0.9878	0.9641	0.9047	0.9735	0.8730

others in most cases, including accurate identification of large vessels and vascular branching structures, while preserving overall vessel connectivity. However, challenges persist in low-contrast regions, such as the over-segmentation observed in CHASEDB1 and the under-segmentation in STARE, as shown in Fig. 4. These areas remain for further refinement.

C. Ablation Study

In this section, we validate the role of key components in our IDA architecture through ablation experiments on the DRIVE → CAM_DB task. Notably, similar conclusions can be drawn from the DRIVE → CHASEDB1 and DRIVE → STARE tasks.

1) *Multi-Resolution Input Strategy*: “Patch Only” refers to the method that uses random patches from the original image as input, while “Whole Only” refers to the method that uses the scaled original image as input. In our MRAT method, both input strategies are used, denoted as “Patch & Whole”. Fig. 5 shows the results for these input strategies. As seen, our multi-resolution input strategy outperforms the other in all metrics,

TABLE V

ABLATIVE RESULTS OF EACH MINI-PATCH SIZE IN OUR MODEL ON THE DRIVE → CAM_DB TASK.

Mini-Patch Size	AUC	ACC	SE	SP	DICE
32	0.9839	0.9589	0.8758	0.9720	0.8532
64	0.9837	0.9581	0.8717	0.9718	0.8503
96	0.9829	0.9561	0.8725	0.9693	0.8444
128	0.9878	0.9641	0.9047	0.9735	0.8730
192	0.9799	0.9529	0.8589	0.9677	0.8325
256	0.9800	0.9511	0.8635	0.9650	0.8283

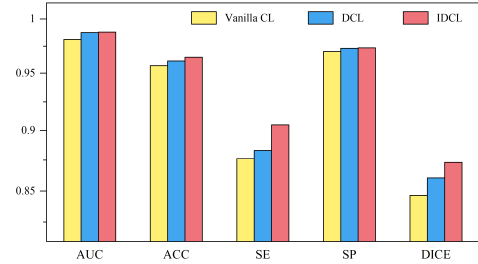


Fig. 7. Quantitative analysis of different contrastive learning methods. **Vanilla CL**: Prototypes are generated from source features, and both domains perform contrastive learning with source prototypes. **DCL**: Prototypes are generated by target-like features, and both domains perform contrastive learning with the target-bias prototypes.

with significant improvements in SE and DICE, where DICE increased by 4.41% and 2.27%, respectively. In addition, the blue arrows in the visualization results of Fig. 6 indicate that our method helps the model capture both the detailed features of vessels and their connectivity, making it more suitable for cross-domain vessel segmentation tasks.

2) *Asymmetric Translation Strategy*: Our MRAT method constructs intermediate images between the source and target domains using CP operations, innovatively employing the Bidirectional Asymmetric Translation (BAT) strategy. Table IV compares the BAT method with other approaches that use Unidirectional Translation (UT) and Bidirectional Symmetric Translation (BST) strategies. Compared to BST and BAT, UT strategy exhibits lower performance due to its unidirectional nature, which neglects the construction of consistent learning strategies for both source and target domains, leading to semantic mismatch. In contrast, our proposed BAT strategy delivers better results, with about 3% improvements in the DICE and SE metrics. Notably, using CutMix to paste target patches onto the source domain and ClassMix to paste source patches onto the target domain (denoted as S2TClass & T2SCut) yields slightly better performance. We attribute this to the higher accuracy of source labels compared to the pseudo-labels, making ClassMix more suitable for source patches. Overall, our method effectively reduces image-level domain shifts.

3) *Selection for Mini-Patch Size*: As shown in Table V, we evaluate the impact of different values of the mask sizes, m , for M_R and M_C in the MRAT strategy on the performance for the DRIVE → CAM_DB task. It can be observed that when the mask size m is set to 128, all metrics achieve optimal performance, with the most significant improvements observed in the SE and DICE metrics. This indicates that the model is

TABLE VI

ABLATIVE RESULTS OF DIFFERENT PROTOTYPE UPDATE STRATEGIES IN OUR MODEL ON THE **DRIVE** \rightarrow **CAM_DB** TASK.

Prototype Weights	AUC	ACC	SE	SP	DICE
0.1	0.9826	0.9556	0.8722	0.9688	0.8428
0.3	0.9828	0.9560	0.8707	0.9695	0.8438
0.5	0.9841	0.9581	0.8791	<u>0.9706</u>	0.8512
0.7	<u>0.9847</u>	<u>0.9582</u>	<u>0.8840</u>	0.9699	<u>0.8524</u>
0.9	0.9833	0.9557	0.8706	0.9691	0.8428
Dynamic	0.9878	0.9641	0.9047	0.9735	0.8730

TABLE VII

ABLATIVE RESULTS OF EACH PRE-TRAINING STRATEGY IN OUR MODEL ON THE **DRIVE** \rightarrow **CAM_DB** TASK.

Random	Self-Cut	VCL	AUC	ACC	SE	SP	DICE
✓			0.9852	0.9601	0.8858	0.9718	0.8583
✓	✓		0.9863	<u>0.9624</u>	<u>0.8926</u>	<u>0.9734</u>	<u>0.8662</u>
✓		✓	<u>0.9876</u>	0.9617	0.8923	0.9727	0.8641
✓	✓	✓	0.9878	0.9641	0.9047	0.9735	0.8730

better able to integrate semantic information from the source and target domains, thus achieving image-level adaptation.

4) Intermediate Domain-guided Contrastive Learning Module: To demonstrate the effectiveness of our IDCL with traditional contrastive learning (where prototypes are generated from source features, and both domains perform contrastive learning with source prototypes, referred to as Vanilla CL) and the domain-interactive contrastive learning (DCL) method in DCLPS [18]. For a fair comparison, all three contrastive learning methods are implemented within the IDA framework proposed in this paper. As shown in Fig. 7, Vanilla CL performs poorly, while our IDCL achieves the best performance. This is because Vanilla CL primarily focuses on enhancing intra-domain class separability but neglects inter-domain class discrepancies, limiting the model’s ability to effectively learn features from the target domain. Although DCL accounts for domain shifts, it directly uses target features for contrastive learning, overlooking the need for consistency between prototypes and features from both domains in the embedding space. In contrast, our IDCL fully utilizes intermediate domain information and establishes a consistent learning strategy for both the source and target domains. This enables the smooth interaction of cross-domain information, resulting in a notable improvement in performance.

5) Selection of Prototype Weights: Considering the uncertainty of pseudo-labels in the target domain, we employ dynamically adjusted prototype weights, $w_{t_{2s}}^{(k)}$ and $w_{s_{2t}}^{(k)}$, in our IDCL. To validate its effectiveness, we compare with several fixed-weight configurations, as shown in Table VI. When the weights are kept too low throughout the training process, it negatively impacts the model’s learning. This is because the prototypes are unable to absorb new knowledge in each iteration, resulting in an under-represented feature. Conversely, when the weights are kept too high, such as when Prototype Weights = 0.9, the presence of false positive pseudo-label errors can introduce considerable noise into the prototypes, thereby

TABLE VIII

ABLATIVE RESULTS OF EACH COMPONENT IN OUR MODEL ON THE **DRIVE** \rightarrow **CAM_DB** TASK.

Pre-train	MRAT	IDCL	AUC	ACC	SE	SP	DICE
✓			0.9822	0.9561	0.8535	0.9723	0.8413
✓	✓		<u>0.9875</u>	<u>0.9624</u>	<u>0.8936</u>	<u>0.9733</u>	<u>0.8664</u>
✓		✓	0.9863	0.9606	0.8821	0.9730	0.8594
✓	✓	✓	0.9878	0.9641	0.9047	0.9735	0.8730

reducing the model performance. Our approach, by considering the predicted probabilities of intermediate images at each iteration, mitigates the impact of incorrect pseudo-labels. Furthermore, it enables the prototypes to fully absorb the intermediate features, leading to improved performance.

6) Choice of Pre-training Strategies: In our default settings, both the student and teacher models are initialized using pre-trained models from the source dataset, with the teacher model’s parameters continuously updated through the EMA strategy. We investigate the impact of different pre-training strategies on the final performance, as shown in Table VII. The “Random” strategy initializes model weights randomly and then trains the model on the source dataset to obtain the pre-trained model. The “Self-Cut” strategy involves applying the multi-resolution CutMix operation exclusively to source images, which can be expressed by the formula $x_{sp} \odot M_R + x_{sr} \odot (\mathbf{1} - M_R)$. The “VCL” strategy implements Vanilla CL within the source domain. Compared to other pre-training strategies, the combination of the “Self-Cut” with the “VCL” proves more effective in enhancing the model performance.

7) Ablation of Different Components: To validate the effectiveness of each component in our method, we conduct ablation experiments, as shown in Table VIII. As demonstrated, our method achieves the best segmentation performance when all components are included, confirming the effectiveness of our approach in mitigating domain gaps at both the image and feature levels.

V. CONCLUSION

In this paper, we propose a novel unsupervised CAM vessel segmentation framework, IDA, which utilizes labeled retinal datasets to assist in the automatic and accurate segmentation of CAM vessels. Our IDA method generates intermediate images through the MRAT strategy to facilitate image-level interaction. To fully leverage the intermediate information, we design a consistent learning strategy for both the source and target domains, using intermediate features to update prototypes that guide domain-wise contrastive learning. This enables intra-class compactness and inter-class separability within domains and allows for feature-level adaptation through cross-domain feature interaction. Extensive experiments on three datasets demonstrate that our method achieves the best performance. In the future, we plan to apply this model to angiogenesis-related research to rapidly provide accurate quantitative parameter characterization.

REFERENCES

- [1] B. Nitzsche *et al.*, “Coalescent angiogenesis—evidence for a novel concept of vascular network maturation,” *Angiogenesis*, pp. 1-11, Feb. 2022.
- [2] C. N. Doukas, I. Maglogiannis, A. Chatziioannou, and A. Papapetropoulos, “Automated angiogenesis quantification through advanced image processing techniques,” in *Proc. IEEE Eng. Med. Biol. Soc.*, 2006, pp. 2345-2348.
- [3] A. Guerra, J. Belinha, N. Mangir, S. MacNeil, and R. N. Jorge, “Simulation of the process of angiogenesis: quantification and assessment of vascular patterning in the chicken chorioallantoic membrane,” *Comput. Biol. Med.*, vol. 136, pp. 104647, Sep. 2021.
- [4] J. Li *et al.*, “Human Non-Small Cell Lung Cancer-Chicken Embryo Chorioallantoic Membrane Tumor Models for Experimental Cancer Treatments,” *Int. J. Mol. Sci.*, vol. 24, no. 20, pp. 15425, Oct. 2023.
- [5] Y. Huang, Z. Zhang, C. Yan, and Q. Lu, “Research on evaluation of CAM image segmentation algorithms on a new database,” in *Proc. Int. Symp. Comput. Inform.*, 2015, pp. 1063-1072.
- [6] D. Hanahan, and R. A. Weinberg, “Hallmarks of cancer: the next generation,” *cell*, vol. 144, no. 5, pp. 646-674, March. 2011.
- [7] Z.-L. Liu, H.-H. Chen, L.-L. Zheng, L.-P. Sun, and L. Shi, “Angiogenic signaling pathways and anti-angiogenic therapy for cancer,” *Signal Transduction Targeted Ther.*, vol. 8, no. 1, pp. 198, May. 2023.
- [8] Y. Zhou, H. Yu, and H. Shi, “Study group learning: Improving retinal vessel segmentation trained with noisy labels,” in *Proc. Int. Conf. Med. Image Comput. Comput.-Assist. Intervent.*, 2021, pp. 57-67.
- [9] A. Galdran, A. Anjos, J. Dolz, H. Chakor, H. Lombaert, and I. B. Ayed, “State-of-the-art retinal vessel segmentation with minimalistic models,” *Sci. Rep.*, vol. 12, no. 1, pp. 6174, Apr. 2022.
- [10] Y. Tan, K.-F. Yang, S.-X. Zhao, and Y.-J. Li, “Retinal vessel segmentation with skeletal prior and contrastive loss,” *IEEE Trans. Med. Imag.*, vol. 41, no. 9, pp. 2238-2251, Sep. 2022.
- [11] J. Staal, M. D. Abràmoff, M. Niemeijer, M. A. Viergever, and B. Van Ginneken, “Ridge-based vessel segmentation in color images of the retina,” *IEEE Trans. Med. Imag.*, vol. 23, no. 4, pp. 501-509, Apr. 2004.
- [12] M. M. Fraz *et al.*, “An ensemble classification-based approach applied to retinal blood vessel segmentation,” *IEEE Trans. Biomed. Eng.*, vol. 59, no. 9, pp. 2538-2548, Sep. 2012.
- [13] A. Hoover, V. Kouznetsova, and M. Goldbaum, “Locating blood vessels in retinal images by piecewise threshold probing of a matched filter response,” *IEEE Trans. Med. Imag.*, vol. 19, no. 3, pp. 203-210, Mar. 2000.
- [14] T.-H. Vu, H. Jain, M. Bucher, M. Cord, and P. Pérez, “Advent: Adversarial entropy minimization for domain adaptation in semantic segmentation,” in *Proc. IEEE/CVF Conf. Comput. Vis. Pattern Recognit. (CVPR)*, Jun. 2019, pp. 2517-2526.
- [15] W. Feng, L. Ju, L. Wang, K. Song, X. Zhao, and Z. Ge, “Unsupervised domain adaptation for medical image segmentation by selective entropy constraints and adaptive semantic alignment,” in *Proc. AAAI Conf. Artif. Intell.*, 2023, vol. 37, no. 1, pp. 623-631.
- [16] Z. Liu, Z. Zhu, S. Zheng, Y. Liu, J. Zhou, and Y. Zhao, “Margin preserving self-paced contrastive learning towards domain adaptation for medical image segmentation,” *IEEE J. Biomed. Health Informat.*, vol. 26, no. 2, pp. 638-647, Feb. 2022.
- [17] B. Xie, S. Li, M. Li, C. H. Liu, G. Huang, and G. Wang, “Sepico: Semantic-guided pixel contrast for domain adaptive semantic segmentation,” *IEEE Trans. Pattern Anal. Mach. Intell.*, vol. 45, no. 7, pp. 9004-9021, Jul. 2023.
- [18] Z. Lu, Y. Zhang, Y. Zhou, Y. Wu, and T. Zhou, “Domain-interactive Contrastive Learning and Prototype-guided Self-training for Cross-domain Polyp Segmentation,” *IEEE Trans. Med. Imag.*, Aug. 2024. Early Access.
- [19] S. Kuang *et al.*, “MSCDA: Multi-level semantic-guided contrast improves unsupervised domain adaptation for breast MRI segmentation in small datasets,” *Neural Netw.*, vol. 165, pp. 119-134, Aug. 2023.
- [20] J. Liu *et al.*, “Unsupervised domain adaptation multi-level adversarial learning-based crossing-domain retinal vessel segmentation,” *Comput. Biol. Med.*, vol. 178, pp. 108759, Aug. 2024.
- [21] Y.-H. Tsai, W.-C. Hung, S. Schultzer, K. Sohn, M.-H. Yang, and M. Chandraker, “Learning to adapt structured output space for semantic segmentation,” in *Proc. IEEE/CVF Conf. Comput. Vis. Pattern Recognit. (CVPR)*, Jun. 2018, pp. 7472-7481.
- [22] Y. Luo, L. Zheng, T. Guan, J. Yu, and Y. Yang, “Taking a closer look at domain shift: Category-level adversaries for semantics consistent domain adaptation,” in *Proc. IEEE/CVF Conf. Comput. Vis. Pattern Recognit. (CVPR)*, Jun. 2019, pp. 2507-2516.
- [23] Y. Yang, and S. Soatto, “Fda: Fourier domain adaptation for semantic segmentation,” in *Proc. IEEE/CVF Conf. Comput. Vis. Pattern Recognit. (CVPR)*, Jun. 2020, pp. 4085-4095.
- [24] F. Lin *et al.*, “Unsupervised Domain Adaptation for Brain Vessel Segmentation Through Transwarp Contrastive Learning,” in *Proc. IEEE Int. Symp. Biomed. Imag. (ISBI)*, May. 2024, pp. 1-5.
- [25] Y. Bai, D. Chen, Q. Li, W. Shen, and Y. Wang, “Bidirectional copy-paste for semi-supervised medical image segmentation,” in *Proc. IEEE/CVF Conf. Comput. Vis. Pattern Recognit. (CVPR)*, Jun. 2023, pp. 11514-11524.
- [26] Q. Ma, J. Zhang, L. Qi, Q. Yu, Y. Shi, and Y. Gao, “Constructing and Exploring Intermediate Domains in Mixed Domain Semi-supervised Medical Image Segmentation,” in *Proc. IEEE/CVF Conf. Comput. Vis. Pattern Recognit. (CVPR)*, Jun. 2024, pp. 11642-11651.
- [27] S. Yun, D. Han, S. J. Oh, S. Chun, J. Choe, and Y. Yoo, “Cutmix: Regularization strategy to train strong classifiers with localizable features,” in *Proc. IEEE/CVF Int. Conf. Comput. Vis. (ICCV)*, Oct. 2019, pp. 6023-6032.
- [28] V. Olsson, W. Tranheden, J. Pinto, and L. Svensson, “Classmix: Segmentation-based data augmentation for semi-supervised learning,” in *Proc. IEEE. Win. Conf. Applic. Comput. Vis. (WACV)*, 2021, pp. 1369-1378.
- [29] Z. Jiang *et al.*, “Prototypical contrast adaptation for domain adaptive semantic segmentation,” in *Proc. Eur. Conf. Comput. Vis. (ECCV)*, 2022, pp. 36-54.
- [30] S. Chaudhuri, S. Chatterjee, N. Katz, M. Nelson, and M. Goldbaum, “Detection of blood vessels in retinal images using two-dimensional matched filters,” *IEEE Trans. Med. Imag.*, vol. 8, no. 3, pp. 263-269, Sep. 1989.
- [31] X. Jiang, and D. Mojon, “Adaptive local thresholding by verification-based multithreshold probing with application to vessel detection in retinal images,” *IEEE Trans. Pattern Anal. Mach. Intell.*, vol. 25, no. 1, pp. 131-137, Jan. 2003.
- [32] I. Liu, and Y. Sun, “Recursive tracking of vascular networks in angiograms based on the detection-deletion scheme,” *IEEE Trans. Med. Imag.*, vol. 12, no. 2, pp. 334-341, Jun. 1993.
- [33] P. Bibiloni, M. González-Hidalgo, A. Mir, and N. Prats-Domínguez, “Vascular Network Analysis with Manual and Automatic Segmentation Using Fuzzy Mathematical Morphology,” in *Proc. 11th Conf. Eur. Soc. Fuzzy Logic Technol. (EUSFLAT)*, 2019, pp. 350-357.
- [34] Z. Yan, X. Yang, and K.-T. Cheng, “Joint segment-level and pixel-wise losses for deep learning based retinal vessel segmentation,” *IEEE Trans. Biomed. Eng.*, vol. 65, no. 9, pp. 1912-1923, Sep. 2018.
- [35] O. Ronneberger, P. Fischer, and T. Brox, “U-net: Convolutional networks for biomedical image segmentation,” in *Proc. Int. Conf. Med. Image Comput. Comput.-Assist. Intervent.*, 2015, pp. 234-241.
- [36] W. Feng *et al.*, “Unsupervised domain adaptation for retinal vessel segmentation with adversarial learning and transfer normalization.” 2021, *arXiv:2108.01821*.
- [37] J. Na, H. Jung, H. J. Chang, and W. Hwang, “Fixbi: Bridging domain spaces for unsupervised domain adaptation,” in *Proc. IEEE/CVF Conf. Comput. Vis. Pattern Recognit. (CVPR)*, Jun. 2021, pp. 1094-1103.
- [38] Y. Cheng, F. Wei, J. Bao, D. Chen, and W. Zhang, “Adpl: Adaptive dual path learning for domain adaptation of semantic segmentation,” *IEEE Trans. Pattern Anal. Mach. Intell.*, vol. 45, no. 8, pp. 9339-9356, Aug. 2023.
- [39] C. Chen, Q. Dou, H. Chen, J. Qin, and P.-A. Heng, “Synergistic image and feature adaptation: Towards cross-modality domain adaptation for medical image segmentation,” in *Proc. AAAI Conf. Artif. Intell.*, 2019, vol. 33, no. 1, pp. 865-872.
- [40] H. Zhang, M. Cisse, Y. N. Dauphin, and D. Lopez-Paz, “mixup: Beyond empirical risk minimization.” 2017, *arXiv:1710.09412*.
- [41] T. Wang, and Q. Dai, “SURVS: A Swin-Unet and game theory-based unsupervised segmentation method for retinal vessel,” *Comput. Biol. Med.*, vol. 166, pp. 107542, Nov. 2023.
- [42] A. Tarvainen, and H. Valpola, “Mean teachers are better role models: Weight-averaged consistency targets improve semi-supervised deep learning results,” in *Proc. Int. Conf. Neural Inf. Process. Syst.*, 2017, pp. 1195-1204.
- [43] I. Loshchilov, and F. Hutter, “Decoupled weight decay regularization.” 2017, *arXiv:1711.05101*.